


# A 118-mW Pulse-Based Radar SoC in 55-nm CMOS for Non-Contact Human Vital Signs Detection

Nikolaj Andersen, *Member, IEEE*, Kristian Granhaug, *Member, IEEE*,

Jørgen Andreas Michaelsen , *Member, IEEE*, Sumit Bagga, *Member, IEEE*, Håkon A. Hjortland, *Member, IEEE*, Mats Risopatron Knutsen, Tor Sverre Lande, *Fellow, IEEE*, and Dag T. Wisland, *Senior Member, IEEE*

**Abstract**—We report a direct-RF pulse-based radar System on Chip (SoC) with applications in vital signs monitoring and occupancy detection. The transmitter complies with FCC, ETSI, and KCC regulatory masks with  $-10$  dB bandwidths of 1.4 and 1.5 GHz centered at 7.29 and 8.748 GHz. The receiver samples the reflected signal at 23.328 GS/s, covering a 9.9-m consecutive range. The measured front-end noise figure is 6.3 dB with 14.7-dB gain at 7.29 GHz. Chest movements from breathing and heartbeats in a human subject were detected at 9 and 5 m, respectively. All required power management and clock functions are integrated on-chip. The SoC was implemented in 55-nm CMOS. In active mode, the system consumes 118 mW from a 1.8-V power supply.

**Index Terms**—CMOS, occupancy detection, radar, System on Chip (SoC), ultra-wideband (UWB), vital signs monitoring.

## I. INTRODUCTION

**R**ADAR-BASED sensors have been used for measuring vital signs, such as breathing and heart rate (HR), since the 1970s [1]. Since then, advances in low-power integrated electronics have enabled a range of compact and inexpensive solutions [2] for applications, such as sleep monitoring and smart building automation for energy saving.

Most commercially available occupancy sensors are based on passive infrared radiation sensors capable of detecting minor movements [3], but lack the ability to detect the presence of stationary subjects [4]. Therefore, continuous-wave (CW)-based Doppler radars have been proposed as an alternative solution, capable of sensing human presence based on vital signs detection [5], [6]. However, CW Doppler radars are only able to measure the velocity of the target. An unambiguous distance measurement is required for sleep monitoring devices to measure the breathing patterns of multiple people

in the same room, and for enabling discrete detection zones in building automation systems. The range resolution,  $\Delta R$ , of a radar quantifies its ability to separate two objects and is proportional to the bandwidth of the transmitted signal

$$\Delta R = \frac{c}{2B} \quad (1)$$

where  $c$  is the speed of light and  $B$  is the transmitter (TX) bandwidth. In order to distinguish multiple targets in a typical vital signs or building automation scenario, a range resolution on the order of tens of centimeter is required, implying gigahertz-range bandwidth.

For peaceful coexistence in the radio spectrum, all radar sensors must comply with regulations for unlicensed operation. In the U.S., the Federal Communications Commission (FCC) allows unlicensed ultra-wideband (UWB) transmission in the 3.1–10.6 GHz band, with average transmitted power less than  $-41.3$  dBm/MHz equivalent isotropically radiated power. Other regulatory bodies offer a narrower, but still sufficient, range of frequencies. This includes the European Telecommunications Standards Institute (ETSI), making available 6.0–8.5 GHz for unlicensed use, as well as Korea Communications Commission (KCC), which allows unlicensed operation in the 7.2–10.2 GHz band.

Wideband radar system architectures suitable for vital signs detection include linear frequency modulated CW radars [7], stepped frequency CW radars [8], and pulse-based radar systems [9], [10]. The wideband nature of these architectures enables target separation while retaining the capability to detect movement based on the phase of the received signal. Compared with pulse-based radars, the CW radar architectures both benefit from a narrow bandwidth at baseband; however, the front-end components still need to accommodate the full bandwidth. Because the TX and receiver (RX) are active at the same time, mitigation is required to avoid degradation of the RX sensitivity. Relevant techniques include separate and directional antennas for TX and RX, applying leakage cancellation techniques, or gating the TX and RX signals [11]–[13]. Furthermore, circuit-level challenges, such as voltage controlled oscillator non-linearity [14], mixer insertion loss, and I/Q imbalance, must be addressed.

Pulse-based radars, on the other hand, transmit narrow pulses with a wide instantaneous bandwidth. The short duration of the transmitted waveform alleviates the TX-to-RX

Manuscript received April 21, 2017; revised July 25, 2017 and September 22, 2017; accepted October 4, 2017. Date of publication November 13, 2017; date of current version November 21, 2017. This paper was approved by Guest Editor Alyosha Molnar. This work was supported by the Research Council of Norway under Project 228794. (*Corresponding author: Jørgen Andreas Michaelsen.*)

N. Andersen, K. Granhaug, J. A. Michaelsen, S. Bagga, H. A. Hjortland, and M. R. Knutsen are with Novelda AS, 0484 Oslo, Norway (e-mail: jorgen@novelda.no).

T. S. Lande is with the Department of Informatics, University of Oslo, 0316 Oslo, Norway.

D. T. Wisland is with the Department of Informatics, University of Oslo, 0316 Oslo, Norway, and also with Novelda AS, 0484 Oslo, Norway.

Color versions of one or more of the figures in this paper are available online at <http://ieeexplore.ieee.org>.

Digital Object Identifier 10.1109/JSSC.2017.2764051

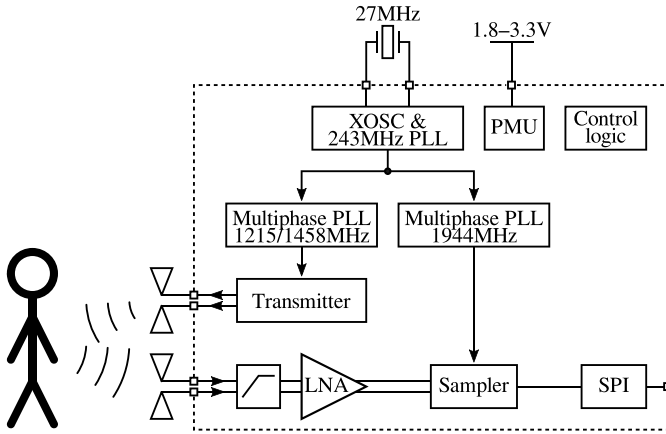


Fig. 1. Block diagram of the radar sensor SoC.

isolation requirement, allowing for systems where the antennas have a wider opening angle, as well as single antenna systems. However, the wide bandwidth makes RX architectures typically found in narrowband systems impractical. One proposed solution to this is the correlation RX, wherein the received signal is multiplied with a template, and the resulting signal is then integrated [15]–[17]. This allows the signal to be sampled at a rate lower than the bandwidth of the actual signal, but in order to track and detect objects the template must be swept in the range of interest, complicating the downstream processing and control logic. Another approach is to directly sample the signal at RF, preserving all the information carried in the received signal in the digital domain. This retains flexibility of choice in subsequent processing and detection algorithms, including the detection of human vital signs by applying FFTs across slow time samples for each range bin, yielding the 2-D range-Doppler matrix, as shown in [18]. The high sampling rate required leads to high power consumption and circuit complexity. In order to mitigate these issues, the slow moving properties of the targets can be exploited by employing non real-time sampling methods, such as the equivalent time sampling (ETS) and swept-threshold (ST) sampling techniques [18]–[22].

In this paper, we report an impulse radar System on Chip (SoC) [23], featuring a TX that complies with regulations for unlicensed operation, direct-RF sampling using the ST technique, and RF interference rejection. The RX samples a 9.9-m consecutive range at 23.328 GS/s, corresponding to 1536 samples. The sampled noise is 2.6 LSB, corresponding to a 6.3-dB noise figure (NF) with 14.7-dB gain at 7.29 GHz.

This paper is organized as follows. In Section II, the system and design aspects are considered. In Section III, implementation details are discussed. In Section IV, measurement results of the system and its building blocks are presented. Conclusions are drawn in Section V.

## II. SYSTEM ARCHITECTURE

A block diagram showing the system architecture is shown in Fig. 1. The TX transmits pulses with an interval given by the pulse repetition frequency (PRF) and after a delay corresponding to the round-trip time of flight (ToF) to the

target and back they appear at the RX, which creates a frame—a digitized representation of the time-domain range profile.

### A. Radar Waveform Design

Waveform design impacts the radar system in several ways: the signal-to-noise ratio (SNR) of the output signal is directly proportional to the energy of the waveform, and the range resolution is proportional to the bandwidth, while the radial velocity resolution is dependent on the signal wavelength [24].

The frequency-shifted Gaussian pulse makes a good candidate for an UWB carrier due to relatively good spectrum filling, short duration in time, and ease of implementation in CMOS. Consider a frequency-shifted Gaussian pulse described by

$$g(t) = p(t) \cos(\omega_c t) = V_{TX} \exp\left(-\frac{t^2}{2\tau^2}\right) \cos(\omega_c t) \quad (2)$$

where  $p(t)$  denotes the Gaussian pulse envelope and  $\tau$  determines the  $-10$  dB bandwidth:  $\tau = (2\pi f_B (\log_{10}(e))^{1/2})^{-1}$ .

For a given bandwidth, the pulse amplitude  $V_{TX}$  is bounded by the regulatory limits for average output power and peak output power [25]. It is not uncommon that the PRF in UWB radar systems employed in short-range scenarios is significantly higher than 1 MHz. Such systems will be bounded by the average power limit only.

Because of the relatively low instantaneous output power, in order to maximize the total transmitted power for any application, the PRF is usually kept as high as possible.

As with any continuous signal with sufficient bandwidth, transmission of UWB waveforms with a constant PRF gives rise to discrete spectral lines at the repetition frequency interval. This is especially apparent when the ratio between PRF and resolution bandwidth used for measurement increases above 1 and can dramatically limit the allowable output power. This effect is mitigated by employing a biphasic-coding modulation scheme, where pulse waveforms of opposite amplitude are transmitted using a pseudo-random noise (PRN) pattern. A typical such output pulse (and its inverse, with the opposite polarity) complying with the generic European UWB regulations is illustrated (Fig. 2) in time and frequency domain.

### B. Swept-Threshold Sampling

The operating principle of ST [22] is shown in Fig. 3. The input signal is compared with a threshold, and the resulting 1-bit quantized value is summed at each range bin to incrementally build the multi-bit frame. The quantization threshold is kept constant while receiving echoes for a given pulse and then stepped in-between radar pulse transmissions, sweeping over a range that covers the input signal plus the input noise. At each range bin, the 1-bit quantized output, after stepping the threshold, approximates the cumulative distribution function (cdf) of the signal, including noise, because the probability of a ‘1’ or a ‘0’ is determined by the underlying cdf.

In practical applications, the required dynamic range can vary significantly depending on the sensor location, the distance to the target, and the presence of large unwanted

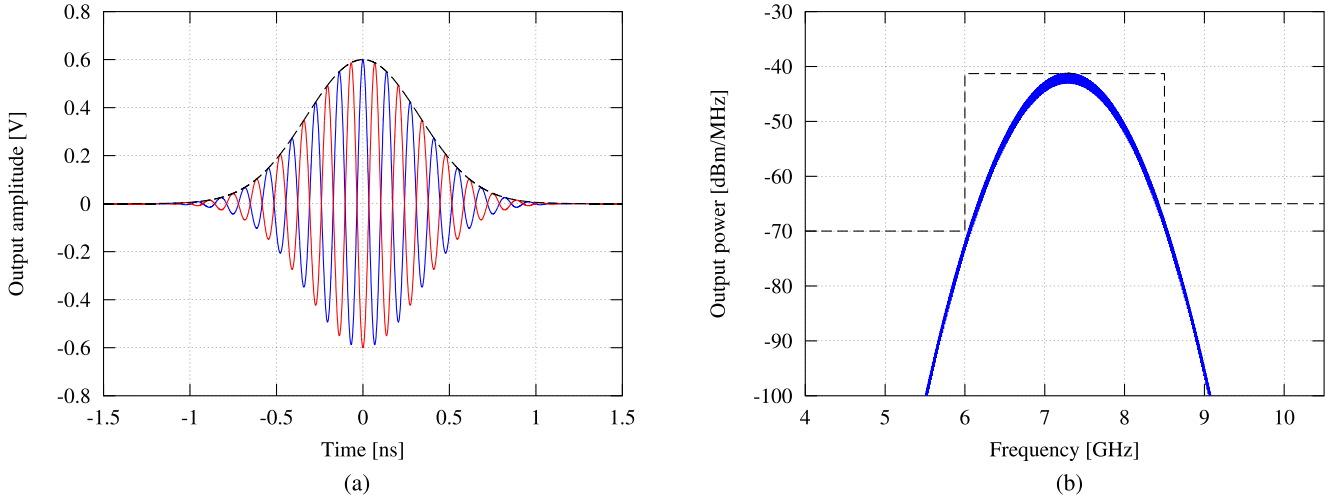


Fig. 2. UWB radar waveform example,  $Z_L = 100 \Omega$ ,  $V_{TX} = 0.6 \text{ V}$ ,  $f_c = 7.25 \text{ GHz}$ ,  $BW = 1.5 \text{ GHz}$ , and  $PRF = 14 \text{ MHz}$ . (a) Frequency-shifted Gaussian in time domain, both polarities. (b) Corresponding frequency spectrum after PRN pattern coding, with ETSI UWB regulatory mask, assuming 6-dBi antenna gain.

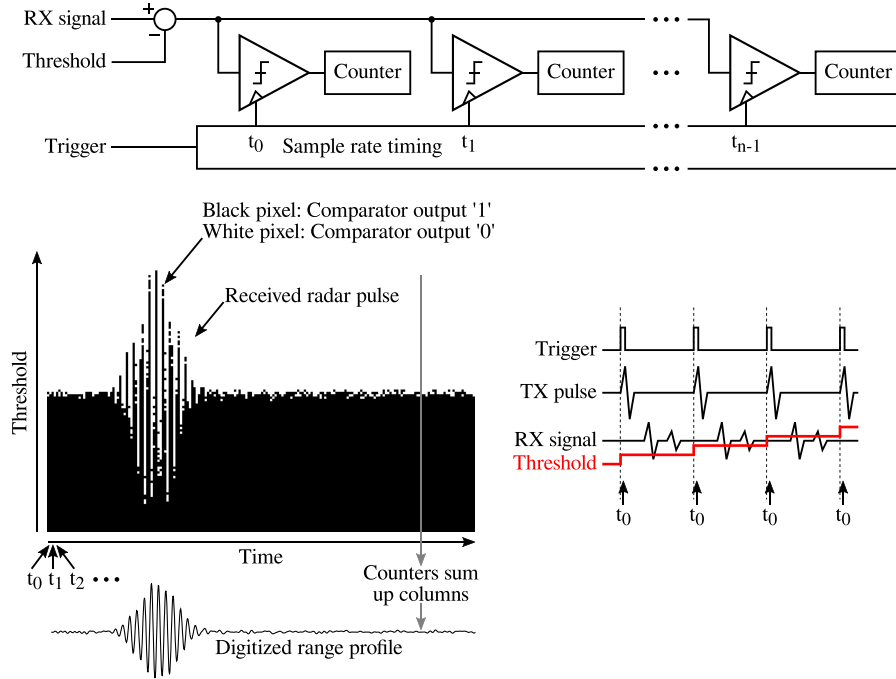


Fig. 3. ST sampling principle.

reflectors close to the targets. The ST sampling introduces a tradeoff where the input range can be traded for sweep times and/or processing gain by adjusting the sweep limits. The sweep time is given by the total number of pulses  $n_{\text{pulses}}$  and the PRF

$$t_{\text{sweep}} = \frac{n_{\text{pulses}}}{\text{PRF}}. \quad (3)$$

The SNR for an ideal pulse-based radar RX from a target given its range  $R$  and radar cross section (RCS)  $\sigma_{\text{RCS}}$  is given by the matched filter radar equation [26]

$$\text{SNR}_{\text{ideal}} = \frac{P_t \cdot t_p \cdot n_{\text{pulses}} \cdot G^2 \cdot \sigma_{\text{RCS}} \cdot \lambda^2}{k_B \cdot T_0 \cdot F \cdot (4\pi)^3 \cdot R^4} \quad (4)$$

where  $G$  is the antenna gain,  $\lambda$  is the wavelength,  $k_B$  is Boltzmann's constant,  $T_0$  is the temperature in Kelvin,  $F$  is the RX noise factor,  $P_t$  is the transmitted pulse power, and  $t_p$  is the pulse duration. The transmitted pulse is approximated as a rectangular windowed pulse with length  $t_p$ , such that the energy of the pulse  $E_p$  equals

$$E_p = P_t \cdot t_p = \frac{V_{TX}^2}{2Z_L} \cdot t_p. \quad (5)$$

In an ST-based pulse radar, (4) becomes

$$\text{SNR}_{\text{ST}} = \frac{P_t \cdot t_p \cdot n_{\text{pulses}} \cdot G^2 \cdot \sigma_{\text{RCS}} \cdot \lambda^2 \cdot G_{\text{ST}}}{k_B \cdot T_0 \cdot F \cdot (4\pi)^3 \cdot R^4 \cdot n_{\text{steps}}} \quad (6)$$

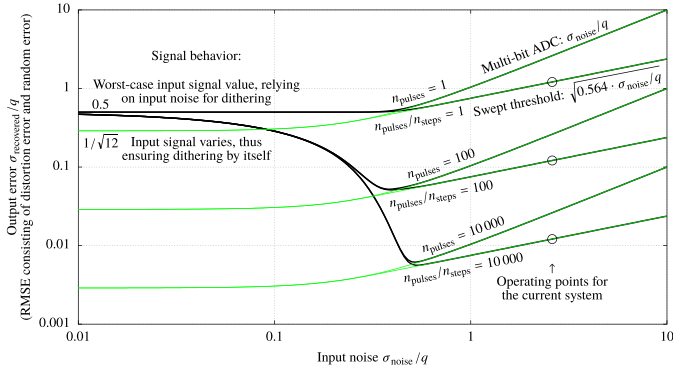


Fig. 4. Numerically calculated output error values from ST and multi-bit analog to digital converter systems plotted against input noise. Asymptote expressions are shown on the left-hand and right-hand sides.

where  $n_{\text{steps}}$  is the number of steps in the threshold sweep, causing an SNR loss, and  $G_{\text{ST}}$  is the SNR gain we get because multiple threshold levels will cover the noise region around the signal value, which will give an integration effect. The threshold sweep range is determined by the largest signal in the sampled frame, which would occur at the minimum distance, plus the noise. Assuming  $5 \cdot \sigma_{\text{noise}}$  is sufficient as the maximum noise voltage, the number of threshold steps required is

$$n_{\text{steps}} \geq \frac{2 \cdot (V_{\text{RX}} \cdot A_{\text{FE}} + 5 \cdot \sigma_{\text{noise}})}{q} - 1 \quad (7)$$

where  $A_{\text{FE}}$  is the voltage gain of the RX front end and where the received pulse amplitude  $V_{\text{RX}}$  is given by

$$V_{\text{RX}} = V_{\text{TX}} \cdot \sqrt{\frac{G^2 \cdot \sigma_{\text{RCS}} \cdot \lambda^2}{(4\pi)^3 \cdot R^4}}. \quad (8)$$

Fig. 4 shows the results of numerical calculations of the performance of ST and multi-bit-analog to digital converter (ADC) systems in the presence of additive white Gaussian noise (AWGN). The expressions written in the plot were extracted from the numerical results. We see that  $\sigma_{\text{noise}}$  should be in the vicinity of or greater than the quantization step  $q$ . For classic multi-bit ADCs, there is a corresponding rule of thumb based on the Widrow quantizing theorem [27]. This choice of step density is shown in Fig. 5 (top). We also find an approximate expression for the ST SNR gain  $G_{\text{ST}}$

$$G_{\text{ST}} \approx 1.772 \cdot \sigma_{\text{noise}}/q. \quad (9)$$

The ST SNR loss can be expressed as

$$L_{\text{ST}} = 10 \cdot \log_{10}(n_{\text{steps}}) - 10 \cdot \log_{10}(G_{\text{ST}}) \quad (10)$$

$$= 10 \cdot \log_{10}((V_{\text{sweep}} + q)/(1.772 \cdot \sigma_{\text{noise}})). \quad (11)$$

Note that for each decibel the input noise in an ST system increases, the output noise from the system will only increase by a half decibel.

We also see that when the sweep range  $V_{\text{sweep}}$  is  $1.772 \cdot \sigma_{\text{noise}} - q$ , we get  $L_{\text{ST}} = 0$  dB, as shown in Fig. 5 (bottom). Note that this is an asymptotic value, since it is assumed that the sweep range is large enough to cover the signal plus the noise. For each doubling of the sweep range beyond this, the ST loss increases by 3 dB.

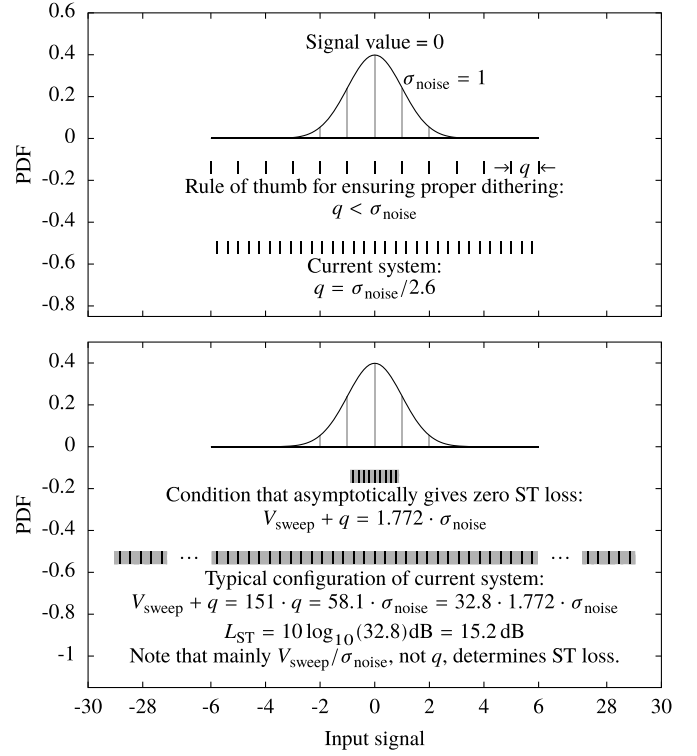


Fig. 5. Top: rule of thumb for deciding the ST quantization step. Bottom: large sweep range causes "ST loss." Shown here is the sweep range that gives zero loss, asymptotically speaking. In practice, such a narrow range would result in strong distortion.

An important advantage of ST compared with multi-bit systems is that we only need a 1-bit quantizer, which simplifies the design and increases the inherent linearity of the system. Another key advantage is that ST can be operated over longer consecutive ranges with no reduction of SNR. In comparison, ETS-based systems use a multi-bit ADC, which is triggered at increasing time offsets, sampling at a single range bin per transmitted pulse. This incurs an SNR loss that is proportional to the number of range bins  $n_{\text{bins}}$  in the sampled frame

$$L_{\text{ETS}} = 10 \cdot \log_{10}(n_{\text{bins}}). \quad (12)$$

Fig. 6 compares the SNR loss of ETS and ST relative to an ideal system for different frame lengths,  $\sigma_{\text{RCS}}$ , and minimum distance. The required ST sweep range is calculated at each minimum distance using (7) and (8). At greater distances and for longer frame lengths, ST compares favorably with ETS. For example, considering a frame length of 1536 range bins and  $\sigma_{\text{RCS}} = 1 \text{ m}^2$ , which is the typical value for a human target [26], ST can operate down to 0.2 m using  $n_{\text{steps}} = 2048$  without clipping the input signal and still show a smaller loss than ETS. In a scenario where the radar is mounted some distance from the target, for example in the ceiling of an office in a building automation application, the performance can be improved by narrowing the sweep range. Using a minimum distance of 0.8 m, a sweep range of 150 steps is sufficient for this system. According to (6), the ST-based system achieves an SNR of  $10 \cdot \log_{10}(\text{SNR}_{\text{ST}}) \approx 22$  dB at 10-m distance using  $n_{\text{pulses}} = 65536$ ,  $t_p = 0.58 \text{ ns}$ , and an NF of 6.3 dB.



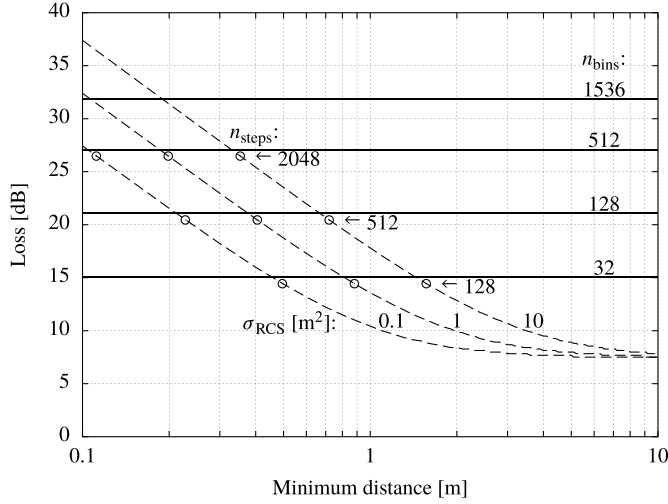


Fig. 6. Comparison of SNR loss in ETS-based systems (solid lines) and ST-based systems (dashed lines) observing targets with different  $\sigma_{RCS}$  values, using  $G = 6$  dBi,  $V_{TX} = 0.6$  V,  $q = 0.3$  mV,  $\sigma_{noise} = 2.6 \cdot q$ , and a low noise amplifier gain of 14.7 dB.

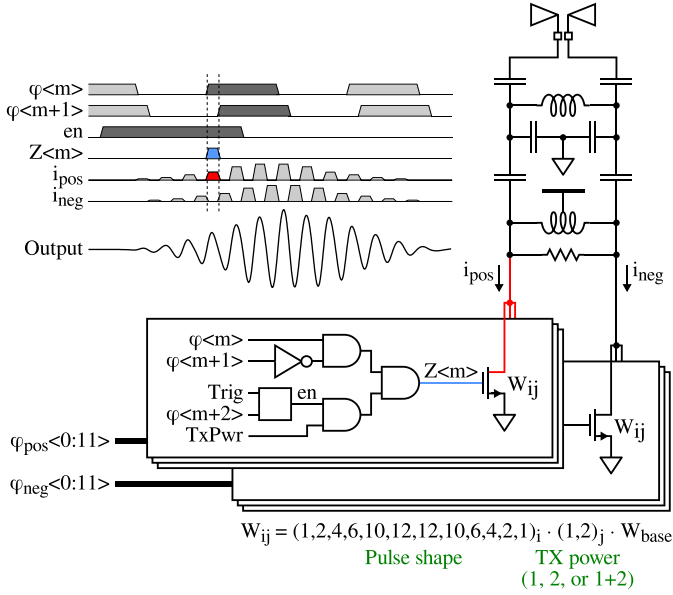


Fig. 7. Pseudo-differential impulse TX, generating pulses with programmable phase, output power, and center frequency.

### III. IMPLEMENTATION

#### A. Transmitter

The short time-duration and low peak power requirement of the waveform makes it a good candidate for a direct synthesis, time domain, digital-intensive implementation, such as [28]. The TX, shown in Fig. 7, is a direct-RF synthesizer generating a sequence of Gaussian-like pulses with programmable PRF, output power, pulse polarity, and center frequency ( $f_c$ ). Two bands of operation are supported,  $f_c = 7.29$  GHz targeting ETSI regulations and  $f_c = 8.748$  GHz targeting KCC regulations, ensuring a broad regulatory footprint through worldwide generic UWB compliance, as both bands also comply with FCC regulations.

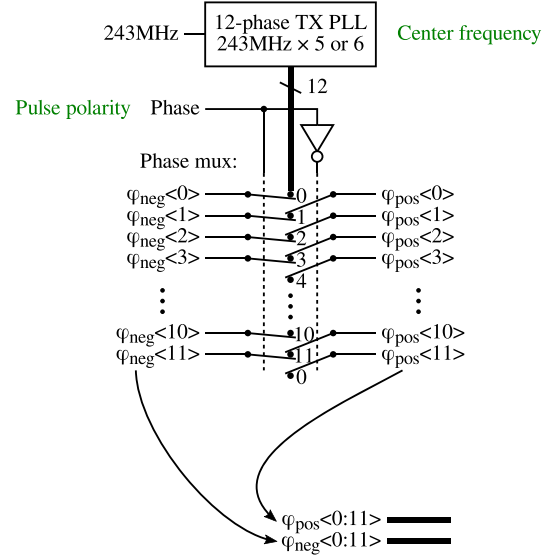


Fig. 8. TX phase-multiplexer, selecting TX-PLL phases for generating pulses of opposite polarity.

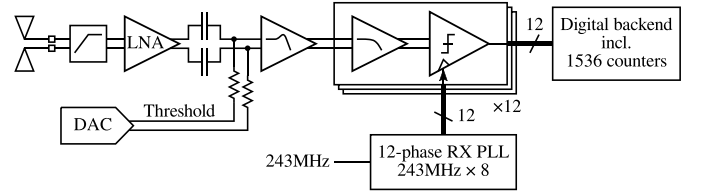


Fig. 9. Block diagram of the RF RX front end.

The transmitted sequence of pulses is biphas-coded using a pseudo-random pattern for spectrum smoothing. The phase multiplexer, shown in Fig. 8, enables the generation of pulses with opposite polarity. The 12 output phases of the TX-phase-locked loop (PLL) are combined through a network of edge combiners into several one-shot pulses driving a distributed output network of individually scaled transistors in sequence, in turn synthesizing an accurately controlled pulse waveform for proper regulatory mask filling. The PLL frequency sets the output center frequency, while the pulse duration relative to  $f_c$  is fixed by the number of active devices in the output network.

The TX is pseudo-differential with different combinations of PLL phases for the positive and negative half circuits. The output network feeds into a differential output load consisting of a real load impedance at the fundamental frequency, shunted by a bandpass filter. The switch-mode network exploits the finite channel resistance and the parasitic capacitance of the devices to synthesize the output envelope. The network is duplicated, and the output devices are scaled to enable programmable peak output power in three discrete steps.

#### B. Receiver

The block diagram of the fully differential RX front end is shown in Fig. 9. It comprises a high-pass filter (HPF), a low noise amplifier (LNA), 12 StrongARM comparators driven by a two-stage pre-amplifier, and a digital to analog converter (DAC) used for setting the quantization threshold.

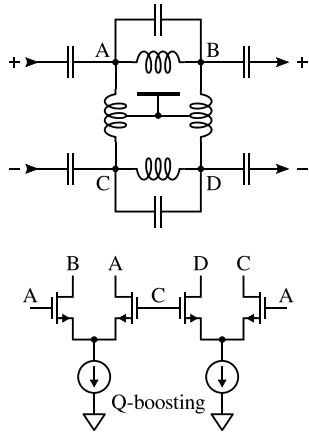


Fig. 10. Passive HPF with active Q-boosting.

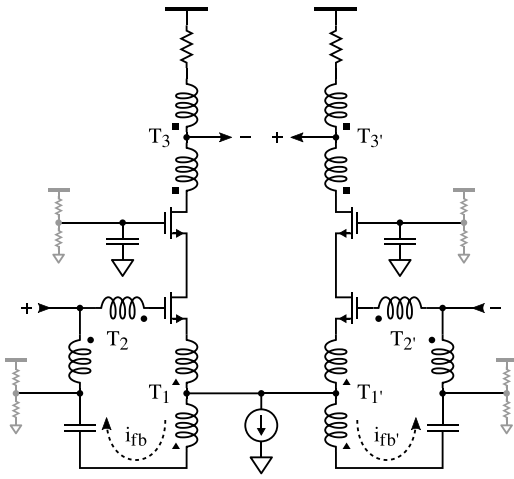


Fig. 11. Frequency-selective power-to-voltage configured LNA with negative reactive current feedback.

The filter attenuates out-of-band interfering signals. As the most prominent source of interference is Wi-Fi operating in the 5-GHz band, an HPF is sufficient for interference rejection in most practical scenarios. While a bandpass filter would add resilience to interference in the upper bands as well, it would require a higher bandwidth in the subsequent amplifying stages, thereby incurring a power penalty. Fig. 10 shows the HPF, which is implemented as a passive single harmonic trap fifth-order elliptic filter. An active Q-boosting circuit is used to enhance the transition band steepness of the filter, allowing its notch to be placed closer to the passband.

The LNA, shown in Fig. 11, is power-to-voltage configured, as the next stage presents a purely capacitive load. The active core of the LNA is a common-source (CS) cascoded amplifier. Wideband impedance and noise matching is achieved by a negative feedback loop around the CS transistor formed by the two auto-transformers  $T_1$  and  $T_2$ . This loop also provides  $g_m$ -boosting [29]. The voltages sensed across the series-connected secondary windings of  $T_1$  and  $T_2$  are mutually coupled to the source- and gate-connected primaries. This results in a gate-source voltage approximately two times the input voltage. The input impedance is given by the transconductance of the

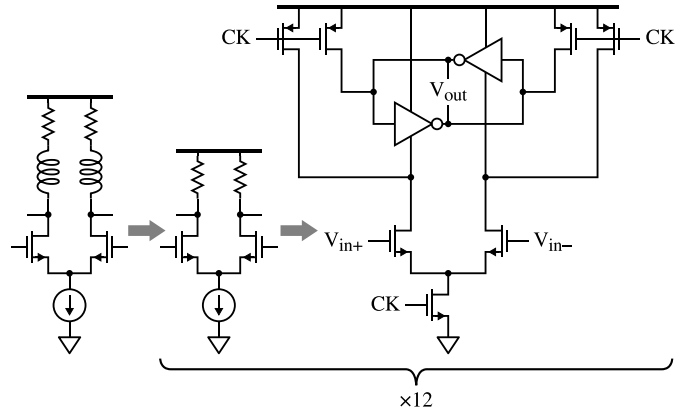


Fig. 12. Buffering, sampling, and 1-bit quantization circuit.

CS transistor taking into account the boosting and the effective turns ratio derived from the self-inductances of  $T_2$  and  $T_1$ . Additionally, the secondary winding of  $T_2$  and the coupling capacitor gives rise to a notch at approximately 3 GHz, further attenuating out-of-band interfering signals. Bridged T-coil peaking is used at the output of the LNA for in-band peaking, realized with auto-transformer  $T_3$ .

A simplified schematic of the time-interleaved 1-bit quantization and sampling circuit is shown in Fig. 12. Twelve comparators are time-interleaved, each clocked at 1944 MHz from a multi-phase PLL, to sample the range profile at 23.328 GHz. The digital backend distributes the comparator outputs to 1536 counters corresponding to a frame length 9.9 m. The counters decode the 1-bit quantized output to a multi-bit output as the sweep progresses and allows for integration by repeating the sweep. The comparators are designed to have a sufficiently narrow aperture to capture signals beyond the front-end bandwidth without requiring sample-and-hold circuits. The second stage of the pre-amplifier is composed of 12 individual amplifiers to isolate kickback noise, and the first stage adds peaking to compensate for the roll-off in the second stage. The combined gain of the two stages of pre-amplifiers is 9 dB.

Previous realizations of ST radar front ends, such as [22], used a continuous-time quantizer with subsequent sampling of the binary value. However, distributing this continuous-time binary valued signal through the required stages of fan-out buffering is challenging and may introduce non-linear distortion. Instead, sampling the signal before quantization allows the use of positive-feedback regenerative gain and deterministic transitions of the digital output relative to the sampling clock.

The TX biphasing is recovered by XORing the comparator outputs with the pseudo-random pattern used for transmission. While the dc offsets arising from mismatch among the interleaved amplifiers and comparators are cancelled by the biphasing, the sampling of the noise is still affected by the mismatch. As the quantization threshold is swept, the amplitude mismatch causes each of the interleaved samplers to sweep through the noise at different points in time. This is shown in Fig. 13. Neighboring samples will therefore be uncorrelated

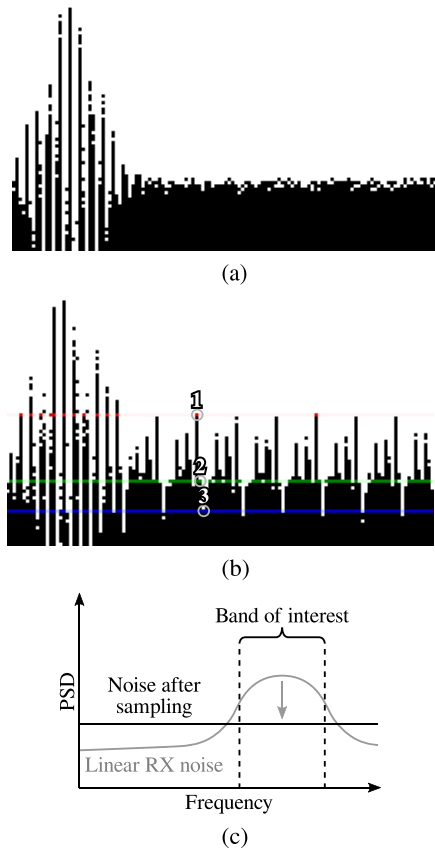


Fig. 13. Amplitude mismatch among the interleaved comparators adds a local random threshold to the ST sampling. Effectively lowering the noise floor inside the band of interest. (a) Received and quantized signal with biphasing enabled. The amplitude mismatch of the interleaved comparators is not apparent. (b) Received and quantized signal with biphasing disabled reveals the amplitude mismatch among the comparators. (c) Randomized threshold added to the comparators translates to sampling the noise at distinct points in time (non-uniform sampling), preserving the noise energy but not the spectral shape from the front end.

for sufficiently large amplitude mismatches. The total noise energy is unaffected, but this decorrelation serves to whiten the sampled noise, thus reducing the in-band noise. This mechanism also applies to interfering signals, spreading their power across the bandwidth of the sampled signal.

While the amplitude offsets are rejected in the quantized output, timing mismatch among the 12 sampling phases gives rise to a fixed-pattern noise that repeats through the frame. Although this degrades the effective number of bits (ENOB) of the quantized output due to added distortion, these artifacts are tolerated by the backend signal processing. The performance is limited by the SNR constituent of the ENOB. In this system, the SNR is characterized in terms of NF, presented in Section IV-A.

The quantization threshold is set by an 11-bit DAC controlled by a digital sweep controller. As the DAC is not required to synthesize an accurate waveform, its implementation is focused on static linearity and settling time only. The sweep controller is clocked by the 243-MHz system clock and steps the DAC at most every other clock cycle, with one clock cycle allocated for settling. The transfer function

from the DAC input is low pass with a low cutoff frequency to reject noise. Furthermore, low-frequency flicker noise will be attenuated by the biphasing at the system level. The quantization in the front end is 1-bit, and therefore inherently linear. The overall static linearity of the conversion is set by the integral non-linearity and differential non-linearity (DNL) of the DAC, and to a lesser extent, the P1 dB of the linear front end. The DAC LSB is required to be on the order of the noise in the front end to allow for processing gain. In this system, some margin is taken as the noise is 2.6 LSB. This does not impact the ST loss because of its contribution to processing gain. However, this requires the DAC to exhibit sufficient DNL. From Fig. 4, we find  $DNL \approx (\sigma_{\text{noise}}/q) - 1$ , which translates to a DNL requirement of  $\pm 1.6$  LSB for the current system. In addition to adequate quantization of the front-end noise, the DAC dynamic range must accommodate  $\sigma_{\text{RCS}}$  set by application level requirements and the combined gain of the HPF and LNA.

The static linearity also contributes to the distortion of the received signal. Typically, a matched filter is used in the subsequent digital signal processing, and the distortion will reduce the detected signal. Therefore, the contribution of the distortion can be seen as reducing the SNR. As such, the system level measurements presented in Section IV-B encompass the non-ideal behavior of the front end and the system as a whole.

### C. Timing Architecture

As shown in Fig. 1, the transceiver timing is derived from a crystal oscillator running at 27 MHz, and a 243-MHz PLL generates a system clock that is used for state machines, and as a common clock for the TX and RX PLLs. Both the TX and RX PLLs have 12 output phases to control the sequencing of the pulse generator in the TX, and for time-interleaving the sampling in the RX. Synchronized timing between the TX and RX is fundamental to the operation of the radar system. Independent TX and RX PLLs allow independent accumulation of local phase noise, which negatively impacts the performance of the radar. However, this arrangement allows for low-frequency clock distribution on-chip. The TX, RX, and digital control logic are separated in the layout to guard against noise coupling and noise injection through the substrate. Also, the system clock can be distributed directly on the PCB for synchronizing multiple radar ICs, a requirement for multi-radar beam steering applications, and can maintain jitter performance comparable to the single radar case. Furthermore, this arrangement allows the center frequency of the generated pulse and the sampling frequency to be chosen independently.

Any phase drift of the RX PLL during the ToF of the pulse adds to the effective sampling jitter. This drift includes phase noise arising from the crystal oscillator and the 243-MHz PLL. However, the phase noise contribution occurs in a time window, and therefore manifests as an N-cycle jitter contribution. Effective sampling jitter converts to sampling noise, which can be a particular problem when large reflectors raise the noise floor and negatively impacts the SNR of smaller

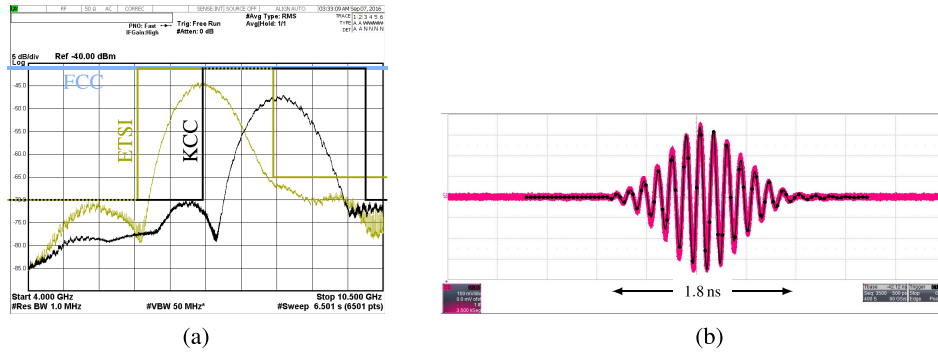


Fig. 14. TX measurement results. (a) Transmitted average output power measured on a spectrum analyzer in a cabled measurement. (b) Transmitted pulses sampled on a high-speed sampling oscilloscope. The corresponding curve sampled by the radar front end is overlaid.

targets at the same range. The worst case rms noise due to jitter is found at the zero crossings and is given by  $V_{J,\max} = 2\pi f_c V_A \sigma_t$ , where  $V_A$  is the peak amplitude of the pulse and  $\sigma_t$  is the effective absolute sampling jitter. A specification for the timing jitter can be derived by introducing the constraint  $V_{J,\max} \leq \sigma_{\text{noise}}$ . Using (8), the largest RCS satisfying the inequality is

$$\sigma_{\text{RCS},\max} = \pi \left( \frac{4R^2 \sigma_{\text{noise}}}{A_{\text{FE}} G \lambda V_{\text{TX}} f_c \sigma_t} \right)^2. \quad (13)$$

Even though the jitter increases with range due to the N-cycle contribution, the reflected power of targets at greater distance is lower due to path loss, negating the increased jitter. The processing gain, however, is unfavorably affected by the increased coherency loss. In the current system, the effective sampling jitter does increase with range [see Fig. 16(b)]. If necessary, the common PLL can be configured to run in a higher power mode, lowering its phase noise to make the N-cycle jitter negligible.

#### IV. MEASUREMENT RESULTS

##### A. RF Measurements

Fig. 14(b) shows the measured time-domain output of the TX captured by a high-speed sampling oscilloscope. In this measurement, the oscilloscope was set to overlay 3500 acquisitions of the 7.29-GHz center frequency pulse with biphasing disabled to capture the repeatability of the output waveform (magenta traces in the plot). Furthermore, the transmitted pulse was sampled using the radar front end in an external loopback configuration. The resulting sampled data were interpolated (black curve), with the original samples presented as dots. The oscilloscope traces are not corrected for attenuation in the measurement setup, and the amplitude of the sampled data is not shown to scale. Fig. 14(a) shows the average output power in dBm/MHz from a cabled measurement for the two center frequencies, corrected for the attenuation in the measurement setup.

The regulatory spectral masks, overlaid in Fig. 14(a), indicate compliance with FCC, ETSI, and KCC in terms of average transmitted power, which by extension, covers most regulatory bodies worldwide. There is some margin to the peak average power limit peak, because the TX is designed

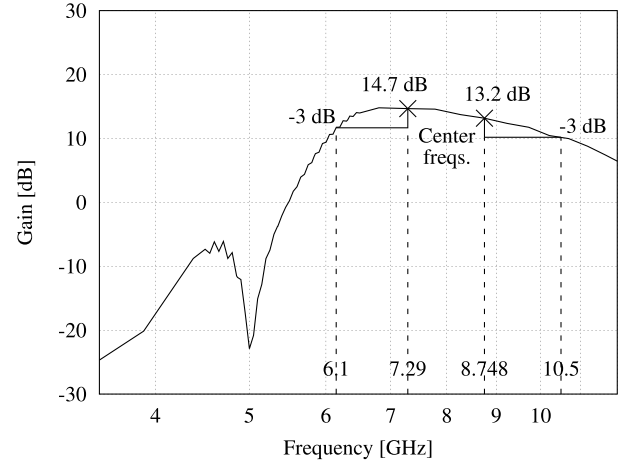


Fig. 15. Measured RX front-end gain.

to take into account an antenna module with approximately 6-dBi gain and further suppression of sidelobes. Mismatch, both between the TX-PLL phases and in the pulse generation network itself, will introduce systematic errors in the resultant waveform, typically increasing the sidelobes of the output spectrum. At the highest output power setting, the measured TX energy consumption is about 85 pJ/pulse.

As the RX is embedded in the radar SoC, the output of the RX front end is not directly observable, and its performance must therefore be estimated from the sampled output of the system. The front-end gain as a function of frequency  $A_{\text{FE}}(f)$  is measured by applying incoherent sine waves to the input port while observing the cdf of the quantized and sampled signal. Assuming the output signal to be a sine wave with harmonics and AWGN, a curve fitting algorithm is used to estimate the amplitude of the fundamental tone of the received signal in units of LSB. The threshold-setting DAC is observable from the test PCB through an on-chip testbus, which allows the LSB,  $q$ , to be measured in volts. The gain is estimated from the applied input power, the recovered amplitude, and the measured LSB, after correcting for attenuation in the measurement setup. Fig. 15 shows the estimated front-end gain. This measurement setup is limited to measuring the combined gain of the HPF and LNA, as it effectively measures



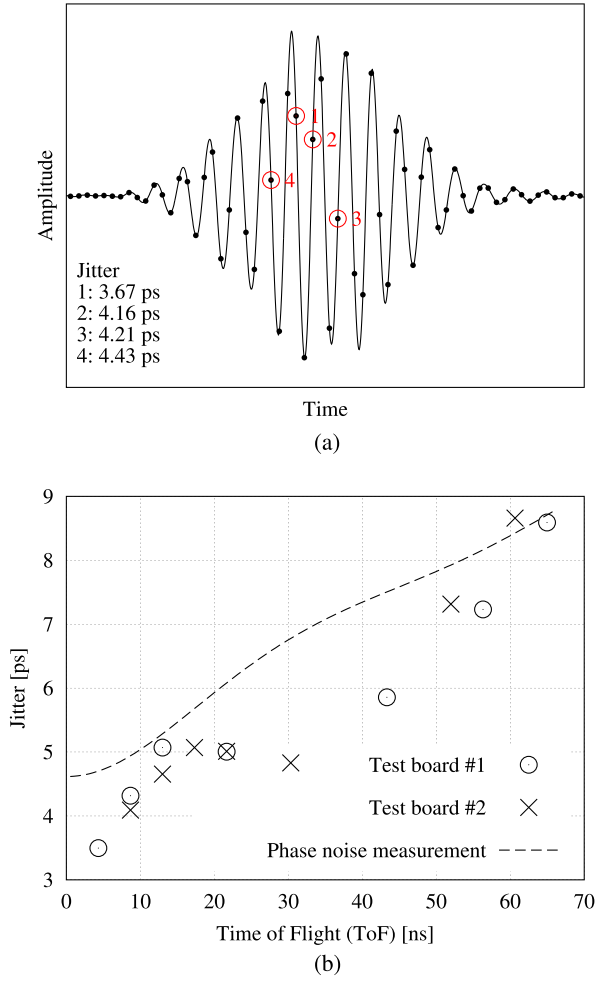


Fig. 16. Sampling jitter measurement results. (a) Effective sampling jitter estimated from the sampled signal. The samples with the highest derivative are used for estimation. (b) Jitter results from sampled data and jitter calculated from measured PLL phase noise.

the ratio of the gain from the RF input to the gain from the DAC input at dc. Thus, peaking in the pre-amp buffer stage adds to the observable gain, while the 9-dB nominal gain in the buffer is not directly measurable, and therefore not included in Fig. 15.

The noise performance of the front end is characterized in terms of spot NF. The total sampled noise  $\sigma_{\text{noise}}$  is assumed to be AWGN due to the noise whitening property of the sampling process. The noise estimate is obtained by sampling with no input signal applied, and the noise histogram is then fit to a normal distribution to estimate  $\sigma_{\text{noise}}$  in units of LSB. The NF is then calculated as

$$\text{NF} = 10 \log_{10} \left( \frac{2 \sigma_{\text{noise}}^2 q^2}{F_s k_B T_0 Z_S A_{\text{FE}}(f)^2} \right) \quad (14)$$

where  $F_s$  is the sampling frequency and  $Z_S$  is the source impedance. Measured results are summarized in Table I.

As shown in Fig. 15, the interference rejection is greater than 20 dB up to 5.1 GHz and greater than 5 dB up to 5.8 GHz. However, a PCB module antenna is co-designed to provide an additional 10-dB rejection at 5.8 GHz.

TABLE I  
NF SUMMARY AT 7.29 GHz

	NF
Linear front-end (simulated)	8.6 dB
System with noise whitening (simulated)	6.0 dB
System with noise whitening (measured)	6.3 dB

TABLE II  
POWER CONSUMPTION BREAKDOWN OF THE RADAR SYSTEM IN ACTIVE MODE

Block	Current consumption
Receiver front-end	42.5 mA
Transmitter	2.7 mA
Digital backend and control	13.8 mA
Clock generation	6.4 mA
Digital I/O	0.2 mA
Total	65.6 mA

Timing jitter converts to amplitude noise proportional to the derivative of the input signal. The effective sampling jitter, including the jitter contribution of the TX, is estimated from transmitted pulses sampled in a loopback configuration using different lengths of cable to simulate the ToF to a target at a given range. The derivative of the sampled and quantized waveform is calculated by oversampling the received signal. The samples with the highest derivatives are chosen for jitter estimation. This is shown in Fig. 16(a). The noise at the chosen samples is estimated from the corresponding cdf. As both the derivative and the noise estimates are in units of LSB, the jitter can be calculated directly without further assumptions about the front end. However, this method does not compensate for coherency loss due to the jitter itself. Fig. 16(b) shows the estimated effective sampling jitter. Fig. 16(b) also shows the estimated sampling jitter calculated from measured phase noise spectra of the PLLs. Phase noise added by off-chip buffering is not deembedded in this result.

### B. System Measurements

The power consumption of the radar system is listed in Table II. When powering the system from the lowest supported supply voltage, 1.8 V, the power consumption is 118.1 mW in full transmit and receive mode without duty cycling. As the SoC is self-contained, this includes low-dropout voltage regulators for core supply, all required clocks for sampling and pulse generation, as well as reference voltages. The RX front end consumes the most power, dominated by the LNA and pre-amplifier stages, and does not depend on the radar configuration. However, both the TX and the digital power consumption depend on the PRF and  $n_{\text{pulses}}$  during range-profile acquisition.

Two application level measurements were set up to measure the vital signs of a human test subject to further evaluate the performance of the radar. In the first measurement, the subject is facing the radar at 5 m and then 9 m while breathing

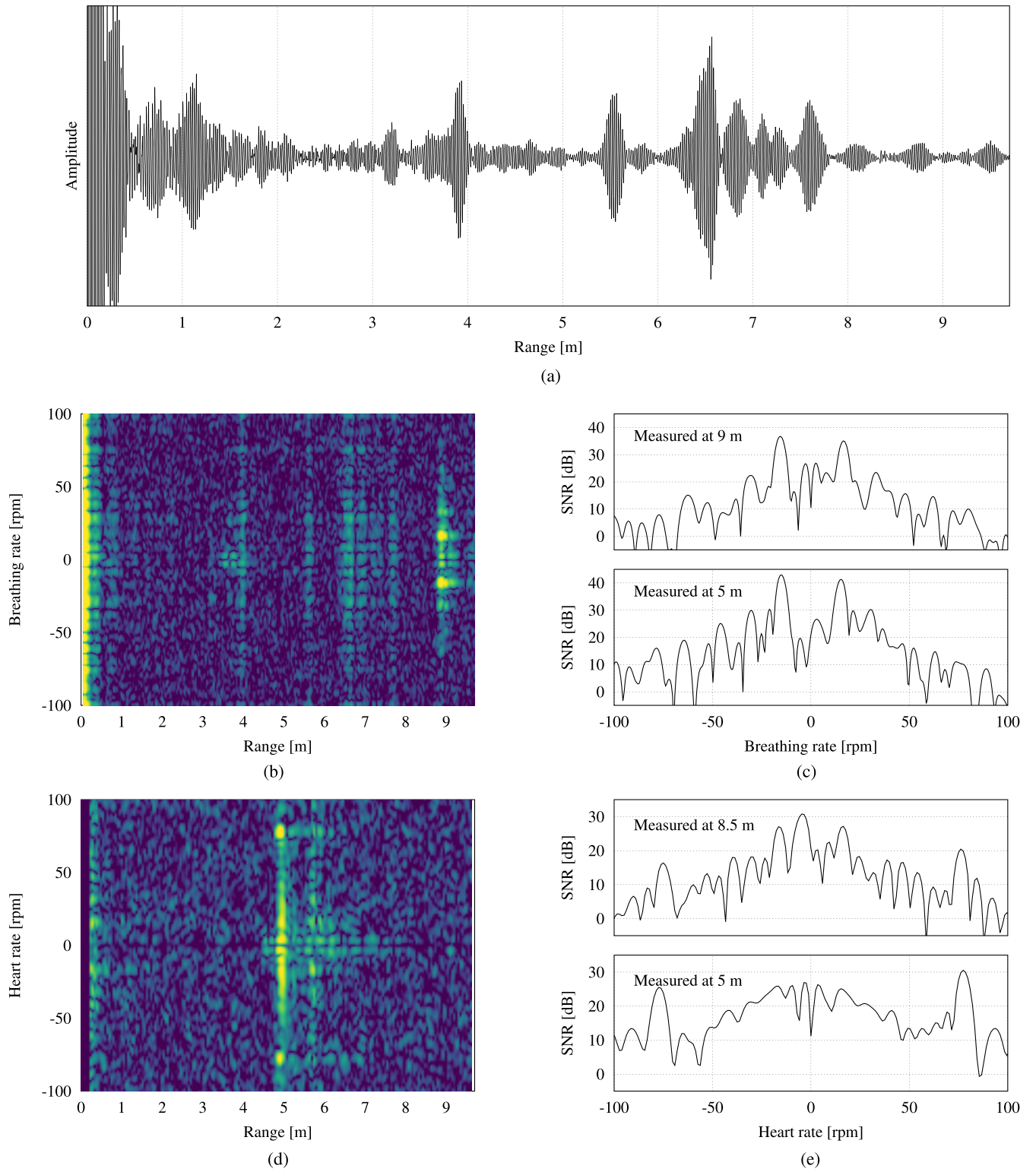


Fig. 17. Vital signs measurement results. (a) Raw range profile with a subject breathing at 9 m. (b) Range-Doppler result from 400 consecutive range profiles sampled at 20 Hz. Chest displacements from inspiration and expiration are visible at approximately 9 m. (c) Doppler plot at approximately 9 and 5 m where the breathing signature is strongest. (d) Range-Doppler result of the heartbeat measurement. The chest displacements due to heartbeats are visible at approximately 5 m. (e) Doppler plot at approximately 8.5 and 5 m where the heartbeat signature is strongest.

normally. In the second measurement, the same subject is again facing the radar, this time at 5 m and 8.5 m while holding his breath in order to get an uncluttered measurement of the heartbeat. The radar SoC was used to capture range profiles,

and the raw data were subsequently post-processed offline into range-Doppler matrices. The RF-sampled range profiles were digitally downconverted to baseband and decimated. 400 consecutive range profiles were used, sampled at 20 Hz.





- [12] G. Wang, J.-M. Muñoz-Ferreras, C. Gu, C. Li, and R. Gómez-García, "Application of linear-frequency-modulated continuous-wave (LFMCW) radars for tracking of vital signs," *IEEE Trans. Microw. Theory Techn.*, vol. 62, no. 6, pp. 1387–1399, Jun. 2014.
- [13] G. Pyo, C. Y. Kim, and S. Hong, "Single-antenna FMCW radar CMOS transceiver IC," *IEEE Trans. Microw. Theory Techn.*, vol. 65, no. 3, pp. 945–954, Mar. 2017.
- [14] A. Anghel, G. Vasile, R. Cacoveanu, C. Ioana, and S. Ciochina, "Short-range wideband FMCW radar for millimetric displacement measurements," *IEEE Trans. Geosci. Remote Sens.*, vol. 52, no. 9, pp. 5633–5642, Sep. 2014.
- [15] D. Zito, D. Pepe, M. Mincica, and F. Zito, "A 90 nm CMOS SoC UWB pulse radar for respiratory rate monitoring," in *IEEE ISSCC Dig. Tech. Papers*, Feb. 2011, pp. 40–41.
- [16] J. Taylor, *Introduction to Ultra-Wideband Radar Systems*. New York, NY, USA: Taylor & Francis, 1994.
- [17] B. Schleicher, I. Nasr, A. Trasser, and H. Schumacher, "IR-UWB radar demonstrator for ultra-fine movement detection and vital-sign monitoring," *IEEE Trans. Microw. Theory Techn.*, vol. 61, no. 5, pp. 2076–2085, May 2013.
- [18] D. T. Wisland, K. Granhaug, J. R. Pley, N. Andersen, S. Støa, and H. A. Hjortland, "Remote monitoring of vital signs using a CMOS UWB radar transceiver," in *Proc. NEWCAS*, Jun. 2016, pp. 1–4.
- [19] C. M. Lai, J.-M. Wu, P.-C. Huang, and T.-S. Chu, "A scalable direct-sampling broadband radar receiver supporting simultaneous digital multibeam array in 65 nm CMOS," in *IEEE ISSCC Dig. Tech. Papers*, Feb. 2013, pp. 242–243.
- [20] H. G. Han, B. G. Yu, and T. W. Kim, "A 1.9 mm-precision 20 GS/s real-time sampling receiver using time-extension method for indoor localization," in *IEEE ISSCC Dig. Tech. Papers*, Feb. 2015, pp. 352–353.
- [21] T.-S. Chu, J. Roderick, S. Chang, T. Mercer, C. Du, and H. Hashemi, "A short-range UWB impulse-radio CMOS sensor for human feature detection," in *IEEE ISSCC Dig. Tech. Papers*, Feb. 2011, pp. 294–296.
- [22] H. A. Hjortland, D. T. Wisland, T. S. Lande, C. Limbodal, and K. Meisal, "Thresholded samplers for UWB impulse radar," in *Proc. IEEE Int. Symp. Circuits Syst.*, May 2007, pp. 1210–1213.
- [23] N. Andersen *et al.*, "A 118 mW 23.3 GS/s dual-band 7.3 GHz and 8.7 GHz impulse-based direct RF sampling radar SoC in 55 nm CMOS," in *IEEE ISSCC Dig. Tech. Papers*, Feb. 2017, pp. 138–139.
- [24] G. Curry, *Radar System Performance Modeling*, 2nd ed. Norwood, MA, USA: Artech House, 2005.
- [25] G. Kolumbán, T. Krébesz, and F. C. M. Lau, "Feasibility of UWB radio: Impulse radio versus chaos-based approach," in *Proc. IEEE Int. Symp. Circuits Syst.*, May 2010, pp. 2450–2453.
- [26] N. Levanon, *Radar Principles*. Hoboken, NJ, USA: Wiley, 1988.
- [27] B. Widrow, I. Kollar, and M.-C. Liu, "Statistical theory of quantization," *IEEE Trans. Instrum. Meas.*, vol. 45, no. 2, pp. 353–361, Apr. 1996.
- [28] T. Norimatsu *et al.*, "A UWB-IR transmitter with digitally controlled pulse generator," *IEEE J. Solid-State Circuits*, vol. 42, no. 6, pp. 1300–1309, Jun. 2007.
- [29] X. Li, S. Shekhar, and D. J. Allstot, " $G_m$ -boosted common-gate LNA and differential colpitts VCO/QVCO in 0.18- $\mu$ m CMOS," *IEEE J. Solid-State Circuits*, vol. 40, no. 12, pp. 2609–2619, Dec. 2005.
- [30] V. C. Chen, F. Li, S.-S. Ho, and H. Wechsler, "Micro-Doppler effect in radar: Phenomenon, model, and simulation study," *IEEE Trans. Aerosp. Electron. Syst.*, vol. 42, no. 1, pp. 2–21, Jan. 2006.
- [31] D. Zito *et al.*, "SoC CMOS UWB pulse radar sensor for contactless respiratory rate monitoring," *IEEE Trans. Biomed. Circuits Syst.*, vol. 5, no. 6, pp. 503–510, Dec. 2011.
- [32] X. Wang, A. Dinh, and D. Teng, "3–10 GHz ultra wideband front-end transceiver in 0.13  $\mu$ m complementary metal oxide semiconductor for low-power biomedical radar," *IET Circuits, Devices Systems*, vol. 8, no. 4, pp. 272–279, Jul. 2014.



**Nikolaj Andersen** (M'14) received the master's degree in microelectronics from the University of Oslo, Oslo, Norway, in 2007.

In 2007, he joined the IC Research and Development Group, Novelda AS, Oslo, where he is currently a Staff IC Design Engineer. In Novelda AS, he has been involved in the design of mixed-signal integrated circuits with a particular focus on the development of radar systems. He has also authored or co-authored several publications.



**Kristian Granhaug** (S'06–M'07) received the M.Sc. degree in electrical engineering from the University of Oslo, Oslo, Norway, in 2006.

Since then, he has been with Novelda AS, Oslo, where he is currently the Vice President of IC design, responsible for integrated circuit design, validation, and test. He has co-authored several publications in the field of direct-RF sampling impulse radar, and holds a number of patents on circuits for time-domain signal processing and ultra-wideband impulse generation.



**Jørgen Andreas Michaelsen** (M'10) received the master's and Ph.D. degrees in electrical engineering from the University of Oslo, Oslo, Norway, in 2006 and 2014, respectively.

In 2013, he joined the IC Research and Development Group, Novelda AS, Oslo, where he is currently a Senior IC Design Engineer involved in high-speed analog and mixed-signal design, including high-speed data conversion for radar systems. He has authored or co-authored several publications. His research in academia

focused on time-domain ADCs.



**Sumit Bagga** (M'12) received the B.E. degree (Hons.) in electrical engineering from Shivaji University, Kolhapur, in 1999, the M.Eng. (Diploma) degree from the Universidade de Brasília, Brasília, Brazil, in 2003, and the Ph.D. degree from the Delft University of Technology, Delft, The Netherlands, in 2009.

He has over 14 years of academic and industrial experience in analog RF IC design. Since 2015, he is a Senior IC Design Engineer with the IC Research and Development Group, Novelda AS, Oslo, Norway, where he is involved in product design of fully integrated radar SoCs for a variety of applications, with design work on direct-RF receive chain. His current research interests include the design of power efficient RF front ends for wireless sensing.



**Håkon A. Hjortland** (S'09–A'11–M'16) received the M.Inf. degree in microelectronics and the Ph.D. degree in natural sciences (microelectronics) from the University of Oslo, Oslo, Norway, in 2006 and 2016, respectively.

He joined the IC Research and Development Group, Novelda AS, Oslo, in 2005, where he is currently a Senior IC Design Engineer. He has authored or co-authored over 30 scientific papers in the field of microelectronics. He is a co-inventor on three issued patents and several pending patents.

His current research interests include IR-UWB radar, custom digital CMOS circuits, 1-bit signal processing, codes, and beamforming.



**Mats Risopatron Knutsen** received the M.Sc. degree from the University of Oslo, Oslo, Norway, in 2010.

Since 2009, he has been with Novelda AS, Oslo, first as an IC Design Engineer, involved in RF and analog design. Later years, he has found interest for antenna and off-chip RF design.





**Tor Sverre Lande** (F'10) is currently a Professor in microelectronics with the Department of Informatics, University of Oslo, Oslo, Norway, and a Visiting Professor with the Institute of Biomedical Engineering, Imperial College London, London, U.K. His primary research interests include microelectronics, both digital and analog. He has authored or co-authored over 150 scientific publications with chapters in three books. His current research interests include neuromorphic engineering, analog signal processing, subthreshold circuit and system design, biomedical circuits and systems, RF CMOS, pulsed radio (UWB), and radar systems.

Prof. Lande has been a technical committee member of several international conferences and has served as a reviewer for a number of international technical journals. He is also a member of other circuits and systems (CAS) technical committees. He is a member of the Norwegian Academy of Technical Sciences. He was the elected Chair of the IEEE Biomedical Circuits and Systems Technical Committee (BioCAS) from 2003 to 2005. He has served as the Technical Program Chair for several international conferences, such as the International Symposium on Circuits and Systems (ISCAS) 2003 in Bangkok, NORCHIP, BioCAS2004, BioCAS2006, BioCAS2010, ISCAS 2011, and ISCAS 2017. In 2006, he was an appointed Distinguished Lecturer of the IEEE CAS Society and an elected member of CAS Board of Governors. He served as the CAS Vice-President of Conferences from 2011 to 2013. He was also the founding Editor-in-Chief of the IEEE TRANSACTIONS ON BIOMEDICAL CIRCUITS AND SYSTEMS from 2007 to 2010. He is serving as an associate editor of several scientific journals and as a guest editor for several IEEE journals.



**Dag T. Wisland** (SM'17) received the M.Sc. and Dr.Scient. degrees in electrical engineering from the University of Oslo, Oslo, Norway, in 1996 and 2003, respectively.

He is currently a Professor with the Nanoelectronics Group, University of Oslo. He was the Head of the Nanoelectronics Group, University of Oslo, from 2004 to 2008. He was a Co-Founder of the semiconductor company Novelda AS, Oslo, and was the CEO from 2004 to 2013 when he was appointed CTO, a position he still holds. He has authored or co-authored several scientific publications and been the principal investigator / project manager for several international research projects. His current research interests include low-power analog/mixedsignal CMOS design, ultra-wideband radio, and the design of ADC/DAC with a particular focus on delta-sigma data converters and new methods and topologies combined with low-power design.

Dr. Wisland serves as a TC Member of the IEEE Circuits and Systems Society Analog Signal Processing and Biomedical Circuits and Systems technical committees.